ACS Sustainable Chemistry & Engineering

pubs.acs.org/journal/ascecg

Research Article

Modular CO_2-to-CO Electrolysis Short-Stack Design—Impact of Temperature Gradients and Insights into Position-Dependent Cell Behavior

Maximilian Quentmeier,* Bernhard Schmid,* Hermann Tempel, and Rüdiger-A. Eichel

Cite This: ACS Sustainable Chem. Eng. 2024, 12, 3876−3885

Read Online

ACCESS | Metrics & More | Article Recommendations | Supporting Information

ABSTRACT: The performance of flow cells for aqueous CO_2-to-CO electrolysis at ambient conditions is reportedly close to meeting industrially applicable rates when operating with membrane electrode assemblies (MEAs) based on anion exchange membranes. However, the challenges of the stacking of these cells are underrepresented in the literature, despite being a major milestone for scaling the technology. Therefore, we report a modular short-stack design for MEA cells and demonstrate its operation with three cells. The short stack replicates the performance of its respective single cell at current densities between 100 and 200 mA/cm^2. At higher current densities (300−400 mA/cm^2), the short stack surprisingly outperforms the single cell showing a lower stack voltage and varying cell voltage depending on the cell's position in the short stack. The temperature distribution affected the membrane conductivity and activation energies for the reactions at the electrodes, which was verified by electrochemical impedance spectroscopy. It could be demonstrated that the temperature distribution is the leading cause of the observed position dependency of the individual cell voltages in the short stack. We show that the inherent asymmetry of the cells results in an asymmetric temperature distribution in the short stack. Taking advantage of the modular stack design, we designed a quasi-symmetric cell eliminating the problem. In this cell, we observed a much smaller voltage variation at 400 mA/cm^2, caused by shunt current, which is well-known from alkaline water electrolysis. In the CO_2 electrolysis short stack, however, their effect was found negligible.

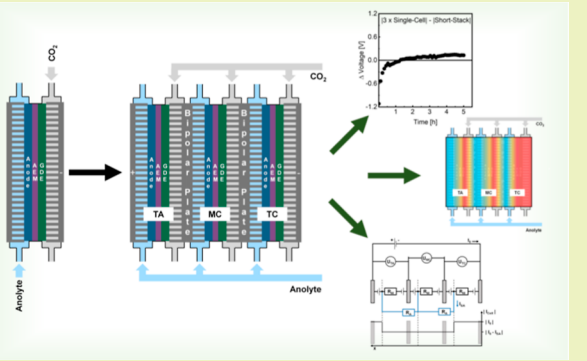

KEYWORDS: *carbon dioxide electroreduction, carbon monoxide, energy conversion, modular stack, membrane electrode assemblies*

INTRODUCTION

Driven by the shift of the chemical industry toward zero-emission processes and the transition of the energy sector to renewable energy sources, CO_2 electrolysis is gaining prominence. In this electrocatalytic process, CO_2 is used as feedstock and is converted to platform chemicals utilizing renewable energy.[1−10] Regarding its technological readiness, the CO_2-to-CO electrolysis performed in lab-scale single flow cells is reported to meet applicable rates.[11,12]

Outstanding efficiencies were demonstrated with membrane electrode assemblies (MEAs), where a gas diffusion electrode (GDE), functioning as the cathode, and a zero gap anode are directly mated on a polymer electrolyte membrane.[13−15] With the MEA, the distance between the electrodes is minimized to the thickness of the membrane, leading to a reduction of transport resistance and thus to an increase in energy efficiency.[13−15] High-performing flow cells, containing the MEA, operate with a single aqueous electrolyte or even only H_2O at the anode.[13−15] Here, the oxygen evolution reaction (OER) takes place, oftentimes on an Ir-MMO catalyst surface which is a stable catalyst for the OER in various conditions.[3,16] The cathode provides a Ag catalyst layer, a highly selective and stable catalyst for the CO_2-to-CO reaction, and is fed with humidified CO_2 gas from the rear side of the electrode.[13−15,17]

Reportedly, the highest selectivities are reached with MEAs containing anion exchange membranes (AEMs). Cation exchange and bipolar membranes have been applied in CO_2-to-CO electrolysis as well.[18−26] Here, high selectivity and high CO_2-to-CO conversion rates have only been demonstrated in GDE-flow cells operating with a buffer layer between the cathode and the membrane. This buffer layer suppresses the competing hydrogen evolution reaction at the cathode caused by the highly acidic environment in a proton-conducting membrane but simultaneously increases the distance between the electrodes and hence decreases the energy efficiency of the flow cell.[18−22,27]

Received: January 22, 2024
Revised: February 9, 2024
Accepted: February 11, 2024
Published: February 22, 2024

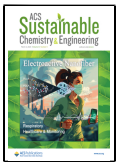

With the AEM, OH^-, HCO_3^-, and CO_3^{2-} ions dominate the ion transport from the cathode to the anode side, which makes the buffer layer redundant.[21,28] The HCO_3^- and CO_3^{2-} ions originate from an undesirable side reaction of the initially formed OH^- ions with excess CO_2.[21,26,29] The CO_2 taking part in this reaction is sometimes considered a lost educt, as the transported ions form CO_2 at the anode, resulting in a CO_2/O_2 mixture that needs to be separated in a supplementary downstream process as well as an increased cell voltage caused by the lower ion conductivity compared to OH^-. On the other hand, the CO_2 removal from the cathode concentrates the product gas, reducing its downstream processing cost.[18,21,30]

The scaling of the MEA cell designs for CO_2 electrolysis, which has received little discussion, is in terms of the high performance of the demonstrated flow cells overdue.[11,14,31,32] Stacking of cells is common in electrolysis processes to perform a scale-up but is associated with several challenges, including the design of cell components such as flow fields and bipolar plates.[14,33,34] These cell components provide mechanical integrity to the cell and function as supporting structures to the MEA. The bipolar plate connects adjacent cells in the stack and thereby serves as a current collector for an anode and a cathode simultaneously.[34]

The architecture of the media flow channels, provided by flow fields and bipolar plates, manages and defines the distribution of media in the cell and thus influences the performance of the cell.[33,34] Different architectures can not only enhance the cells' performance but also impact the heat accumulation in cells and stacks. Temperature management, which is a more obvious task in the stack than in a single cell due to greater input of power, needs to be considered in the stacking of an electrolyzer.[11,33−35]

Moreover, the distribution of the electrolyte via manifolds influences the stack performance by enabling the formation of shunt currents.[36,37] When assembling a stack, individual cells are connected in series, while the media are supplied in parallel to the cells. This is a common practice, as the electrical connection in series leads to high stack voltages instead of high current, resulting in lower ohmic losses in the periphery. On the other hand, the media and educts need to be supplied in parallel to ensure identical conditions in all cells. Most of the applied current flows through the active area of the stack, but some current can flow through the electrolyte, which provides a parallel path to the current flowing in the stack. These shunt currents flow via the electrolyte between the two terminal cells in the stack [terminal cathode (TC) and terminal anode (TA)], leading to lower current densities in the middle of the stack. This uneven distribution of current density between the individual cells in the stack can diminish the cell performance and accelerate degradation processes.[37]

Regarding the stacking in CO_2-to-CO electrolysis, the functionality of a short stack with multiple MEA cells, operating with 1 M KOH as anolyte at elevated temperatures (50 °C) under different pressure conditions, has been successfully demonstrated.[14]

However, the stacking of CO_2 electrolyzers is underrepresented in the literature, despite being a critical aspect of scaling the technology. Our work reports a three-cell short stack for MEA cells operating at ambient conditions with a low-conductivity anolyte (10 mM $KHCO_3$) to minimize the risk of salt precipitation and shunt current formation. To ensure high flexibility while at the same time increasing the complexity of the system by stacking the cells, we introduce a modular design. The performance of the short stack as well as the performance of the individual cells in the short stack is evaluated and compared to the equivalent single cell.

MATERIALS AND METHODS

The short stack was assembled with two bipolar plates and two end plates, each of them providing a serpentine media flow channel similar to the flow fields presented in our previous work.[33] The single cells contained two end plates. The end plates and bipolar plates were manufactured from Ti (grade 1). PTFE sheets with a rectangular window of 10 cm^2 were integrated to seal the cells around the electrodes and function as insulators. A cathode with a Ag catalyst layer and anode with an Ir-MMO catalyst layer for carbon dioxide electrolysis were purchased from Dioxide Materials[13] and used in a size of 10 cm^2. The electrodes were mounted on a Sustainion X37−50 grade RT AEM, purchased from Dioxide Materials.

A 10 mM $KHCO_3$ anolyte solution was prepared with ultrapure water (ELGA PURELAB flex) and $KHCO_3$ (Honeywell Fluka) and was circulated via a peristaltic pump with a volume flow of 50 and 150 mL/min through the single cell and short stack from vessels containing 250 and 500 mL of the electrolyte, respectively.

The product gas from the cathode was analyzed via a Trace 1310 Thermo Scientific gas chromatograph and quantified with a drum-style gas counter (RITTER). Electrical measurements were performed with a PGSTAT302N potentiostat (Metrohm). Further information on the used materials and devices can be found in the Supporting Information.

Experiments were conducted in two systems: (1) a single cell and (2) a three-cell short stack. For both systems, experiments were performed at 200 mA/cm^2 for 300 min. Additionally, the current density was stepwise increased from 100 to 200, 300, and 400 mA/cm^2. Each current density was applied for 100 min. For each current density step, a galvanostatic electrochemical impedance spectroscopy (EIS) measurement was performed under load in a frequency range from 40 kHz to 100 mHz and an amplitude of 10% of the applied current density.

In all experiments, the CO_2 supply was adjusted to the experimental parameter λ, which was introduced by researchers and already used in our previous work.[33,38] To provide a sufficient CO_2 supply to the cell, $\lambda = 5$ was applied in all experiments.

To characterize the single cell and the short stack, the listed performance indicators were utilized: (1) Faraday efficiency for CO [FE(CO)] of the single cell, (2) FE(CO) of the complete short stack, as all the entering and exiting gas shared the same manifold in the short stack, (3) single-cell voltage, measured between the anode and the cathode, (4) short-stack voltage, measured between the anode of the TA and the cathode of the TC, (5) voltage of the individual cells in the short stack, measured between the anodes and cathodes of the respective cells, and (6) electrical energy input efficiency (ϵ_{CO}), which is calculated via the free Gibbs energy ($\Delta G_{CO} = 255$ kJ/mol), the cell voltage (U_{Cell}), the Faraday constant (F), and the number of electrons participating in the CO_2-to-CO reduction reaction ($z = 2$).

$$\epsilon_{CO} = \frac{\Delta G_{CO} \cdot FE(CO)}{z \cdot F \cdot U_{Cell}} \quad (1)$$

To facilitate the comparison of the single-cell and short-stack voltages, the differential voltage (Δvoltage) between the absolute value of three times single-cell voltage ($U_{single\ cell}$) minus the absolute value of the short-stack voltage ($U_{short\ stack}$) is used (eq 2). A value of zero corresponds to the same performance of the short stack and single cell regarding the cell voltages.

$$\Delta voltage = 3 \cdot |U_{single-cell}| - |U_{short-stack}| \quad (2)$$

For better readability of the text, tables with the values of the defined figures of merit and the high-frequency resistance (HFR) obtained in experiments are provided for the single-cell (Table 1) as well as for the short-stack experiments (Table 2).

https://doi.org/10.1021/acssuschemeng.4c00630
ACS Sustainable Chem. Eng. 2024, 12, 3876−3885

Table 1. Values of Performance Indicators and HFR Obtained in Experiments with the Single Cell

j [mA/cm^2]	FE(CO) [%]	U [V]	$\epsilon_{(CO)}$ [%]	T_{EI} [°C]	HFR [Ω·cm^2]
		single cell			
100	94.85	−2.88	43.52	27	1.61
100	95.96	−2.88	43.94	30	1.53
200	93.97	−3.01	41.25	30	1.28
200	92.22	−3.02	40.26	33	1.21
300	91.85	−3.41	35.59	33	0.86
300	90.28	−3.15	37.85	36	0.79
400	85.75	−3.77	30.06	38	0.95
400	81.45	−3.36	32.05	43	0.90

RESULTS AND DISCUSSION

The investigated systems were assembled with in-house-designed end plates and bipolar plates, which are illustrated in Figure 1a. The media were delivered to the serpentine channels via media flow channels on the rear side of the components, to enable the stacking of the cells and to establish a plane contact surface for seals and electrodes. It is noteworthy that the bipolar plate contained two of the plates illustrated in Figure 1a(right), giving the bipolar plate a modular characteristic. Furthermore, the bipolar plates possess a jetty to enable the voltage measurement of the individual cells in the short stack. Thus, in addition to the performance of the full three-cell short stack, the performance of the individual cells could be evaluated and compared to the performance of the respective single cell. In Figure 1b,c, an illustration and an image of the investigated short stack are presented.

Electrochemical Experiments. The results of the electrochemical experiments at 200 mA/cm^2 with the single cell and the short stack are illustrated in Figure 2. The voltages of the single cell (Figure 2a), the short stack (Figure 2b), and the individual cells in the short stack (Figure 2c) are given over time. FE(CO) values for the single cell and the short stack are shown in Figure 2a,b. To compare the voltages of the short stack and the single cell, the Δvoltage is illustrated in Figure 2d over time.

The obtained results demonstrate a stable process of the single cell and the short stack at 200 mA/cm^2 for 300 min. In both experiments, FE(CO) was maintained over 90%. We emphasize that no other product than CO and H_2 was observed in relevant amounts. The results of ^{1}H NMR analysis measurement of an anolyte sample are provided in Figure S3, and the total FE determined in experiments with the short stack and the single cell at different current densities is provided in Figure S1 in the Supporting Information.

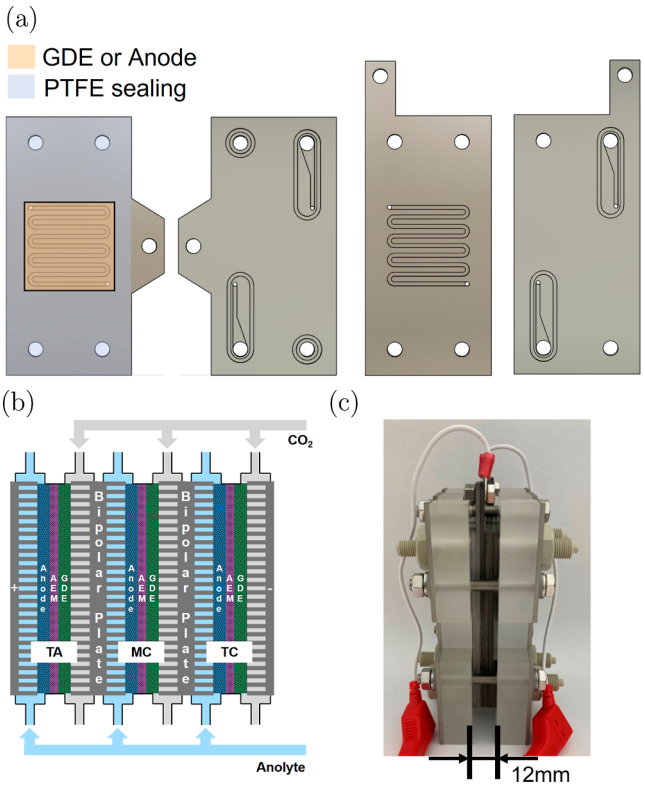

Figure 1. (a) Illustration of the front and rear side of end plates including the indicated position of the PTFE sealing and the GDE (left); illustration of the front and rear side of a modular bipolar plate (right), (b) illustration of the three-cell short stack, and (c) image of the three-cell short stack.

For the single cell, a cell voltage of 3 V and for the short stack, a stack voltage of 9 V were observed. The voltage measurements of the individual cells showed values similar to the ones determined for the single cell (3 V). It is noteworthy that a difference between the individual cells was observed. The TA operated at cell voltages higher than those of the middle cell (MC), and the voltage of the TC was observed to be the lowest of all three individual cells. The short-stack voltage is the sum of the individual cell voltages, and since these are similar to the single-cell voltage, Δvoltage is close to zero (Figure 2d). 2 hours after the start of the experiment, Δvoltage shifts from a negative to a positive value and remains positive for the rest of the experiment. This behavior of Δvoltage indicates that the individual cells in the short stack operate on average, after an initial phase, at lower cell voltages

Table 2. Values of Performance Indicators and HFR Obtained in Experiments with Short Stacks

j [mA/cm^2]	FE(CO) [%]	U [V]	U_{TC} [V]	U_{MC} [V]	U_{TA} [V]	$\epsilon_{(CO)}$ [%]	HFR [Ω·cm^2]
			regular short stack				
100	95.85	−8.38	−2.79	−2.79	−2.82	45.34	3.26
200	93.61	−8.87	−2.95	−2.96	−2.96	41.38	2.41
300	90.97	−9.29	−3.02	−3.12	−3.15	38.82	2.48
400	83.17	−9.75	−3.16	−3.30	−3.30	33.82	2.58
			short stack with an additional cooling plate				
100	95.58	−8.66	−2.90	−2.91	−2.87	43.74	
200	93.80	−9.13	−3.04	−3.04	−3.05	40.71	
300	92.55	−9.29	−3.13	−3.10	−3.14	39.49	
400	85.98	−9.77	−3.26	3.19	−3.32	34.86	

https://doi.org/10.1021/acssuschemeng.4c00630
ACS Sustainable Chem. Eng. 2024, 12, 3876−3885

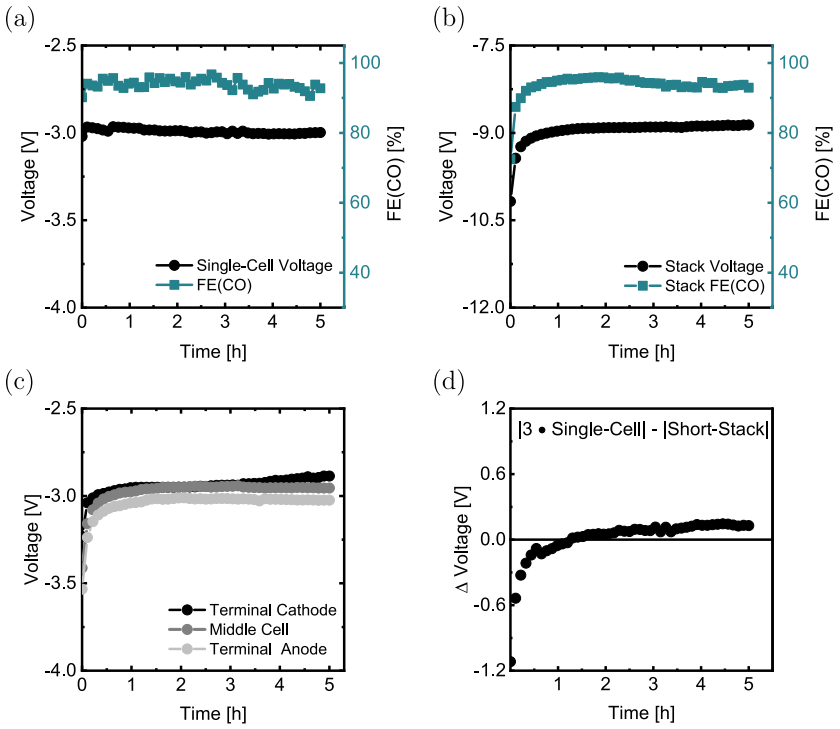

Figure 2. Over time at 200 mA/cm^2: cell voltage and FE(CO) for the (a) single cell and (b) short stack, (c) cell voltages of individual cells in the short stack, and (d) differential voltage between the absolute value of three times single-cell voltage minus short-stack voltage.

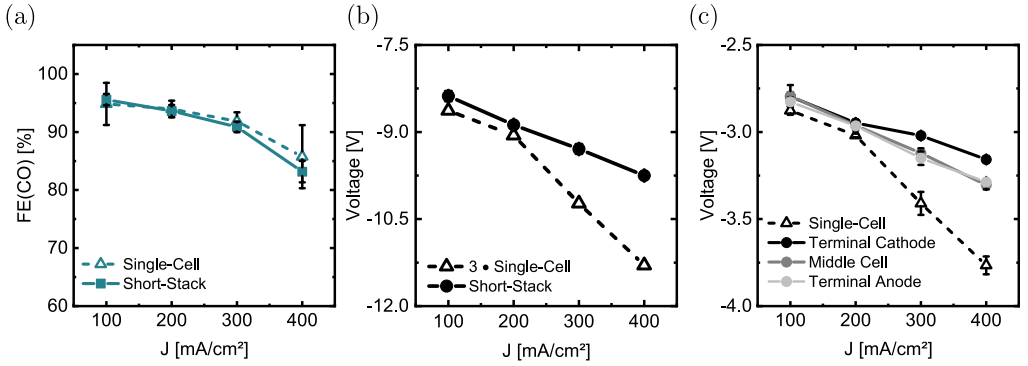

Figure 3. Over different current densities: (a) FE(CO) of the single cell and short stack, (b) stack voltage and three times single-cell voltage, and (c) voltages of single cell and individual cells in the short stack.

than those of the single cell. Regarding these results, the designed short stack resembles the single-cell performance at 200 mA/cm^2.

It is noteworthy that the determined cell voltages as well as the FE(CO) for the discussed current density are consistent with values given in the literature for MEAs operating with the same material. Accordingly, the electrical energy input efficiency for the single cell ($\epsilon_{(CO)}$ = 41.25%) and the short stack ($\epsilon_{(CO)}$ = 41.38%) is in alignment with the literature. Thus, the performance of this stack is approaching the theoretical maximum of $\epsilon_{(CO)}$ = 62% for alkaline CO_2-to-CO reduction coupled with the OER as recently discussed by Reichbauer et al.[12]

The results obtained at current densities from 100 to 400 mA/cm^2 for the single-cell and short-stack ion are illustrated in Figure 3. Figure 3a provides the FE(CO) for the single cell and the short stack. Figure 3b illustrates the stack voltage and the value of three times the single-cell voltage, and Figure 3c depicts the single-cell voltage and the voltage of the individual cells.

For both systems, an increasing voltage and a decreasing FE(CO) can be observed with increasing current density due to the increasing current load passing through the systems (Figure 3b). From 200 to 400 mA/cm^2, the curves are linear, indicating that the ohmic resistance of the cell dominates the cell voltage in this regime. While FE(CO) for the single cell and the short stack shows similar behavior by decreasing from 95% (100 mA/cm^2) to 85% (400 mA/cm^2), the voltages differ in behavior. The voltage of the single cell increases from 2.85 V at 100 mA/cm^2 to 3.6 V at 400 mA/cm^2. For the individual cells of the short stack, a similar cell voltage of 2.82 V at 100 mA/cm^2 was observed; however, higher cell voltages compared to the single cell were observed at higher current densities. For instance, at 400 mA/cm^2, cell voltages of 3.3, 3.3, and 3.2 V were determined for the TA, the MC, and the TC, respectively. Hence, the performance of the individual cells in the short stack differs from the performance of the single cell at higher

https://doi.org/10.1021/acssuschemeng.4c00630
ACS Sustainable Chem. Eng. 2024, 12, 3876−3885

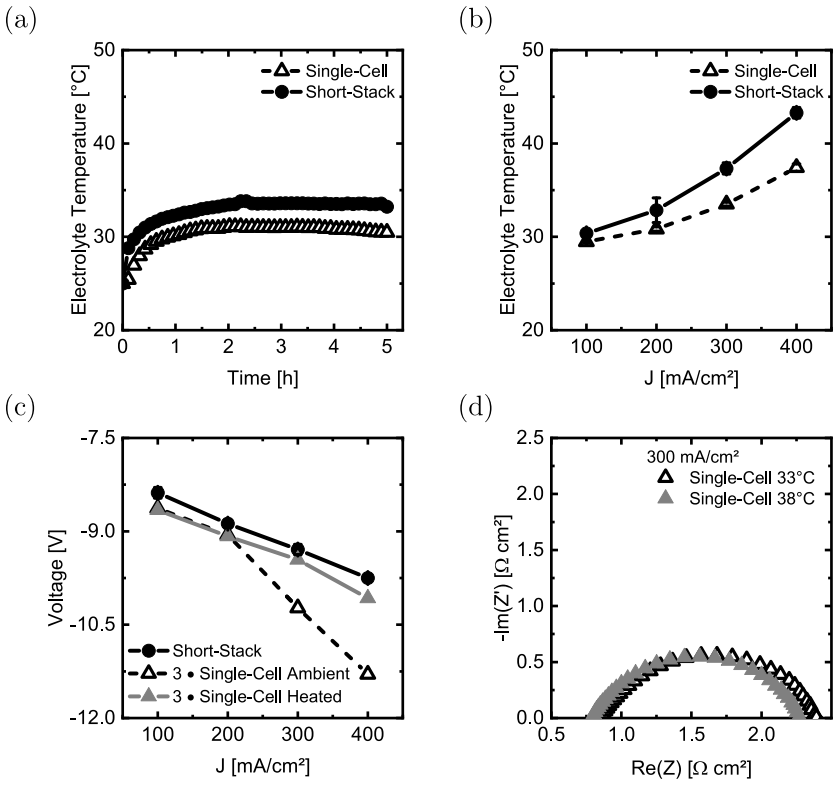

Figure 4. (a) Electrolyte temperature in experiments with single cell and short stack at 200 mA/cm^2 over time, (b) electrolyte temperature in experiment with single cell and short stack over different current densities, (c) single-cell voltage determined in experiments with a heated electrolyte (30 °C at 100 mA/cm^2; 33 °C at 200 mA/cm^2; 38 °C at 300 mA/cm^2; 43 °C at 400 mA/cm) versus single-cell voltage determined at ambient conditions and stack voltage over applied current densities, (d) Nyquist plots for the single cell obtained at 300 mA/cm^2 with a 300 mA excitation amplitude, in experiment at ambient conditions (33 °C) and in experiment with the heated electrolyte (38 °C).

current densities. It is noteworthy that at all current densities, the lowest cell voltage was consistently observed for the TC.

Considering the stack voltages, the results obtained indicate a performance-increasing effect of the short stack. In contrast to the free-standing single cell, the cells in the short stack touch each other with most of their surface area. Since each cell generates heat, a different behavior of the temperature development in these two systems can be anticipated.

Temperature Effects. The ion conductivity of AEMs is temperature-dependent and oftentimes lower for HCO_3^- and CO_3^{2-} ions than for OH^- ions.[13,26,39−43] For instance, the ionic conductivity of the Sustainion membrane increases from 24 mS/cm at 25 °C to 66 mS/cm at 80 °C when operating with 1 M $KHCO_3$.[13,39] As the ionic conductivity of the membrane increases at elevated temperatures, it is reasonable to assume that temperature effects lead to an increase of the individual cell performances.

Illustrated in Figure 4a,b are the temperatures measured in the electrolytes for the single cell and the short stack. In Figure 4a, the temperatures measured in experiments at 200 mA/cm^2 (Figure 2) are illustrated over time. The electrolyte temperatures increase at the beginning of the experiment from 25 °C and reach a steady state after 1 h. In experiments with the single cell, the electrolyte reaches a temperature of 30 °C and with the short stack, a temperature of 33 °C was measured toward the end of the experiment. Figure 4b depicts the temperatures determined in experiments at different current densities. The electrolyte temperatures increase with increasing current densities and reach values of 38 °C (single cell) and 43 °C (short stack) at 400 mA/cm^2.

The plateau formation of the electrolyte temperatures over time at 200 mA/cm^2 indicates that an equilibrium between the cooling of the systems and the production of heat from ohmic losses and the reaction of OH^- with excess CO_2 is reached. In terms of the difference in steady-state temperatures for the single cell and the short stack, the periphery of the systems needs to be considered. For the single cell, a smaller electrolyte vessel is used compared to the short stack. On one hand, the larger electrolyte vessel provides a larger surface area for cooling. On the other hand, a longer retention time of the electrolyte in the vessel can be calculated via the electrolyte volume flows for the single cell (5 min single cell; 3.5 min short stack). Regarding the applied electrolyte flow rates, a similar volume flow is anticipated for the individual cells and the single cell, enabling similar cooling of each cell. The discussed factors can have an impact on the temperature development in the different systems; however, it is plausible that the ratio of the active surface area to the exterior surface area, which is exposed to the air, has a more significant influence. In the short stack, the active surface area triples compared to the single cell, while the exterior surface area remains practically the same. Thus, a significantly increased amount of heat occurs at the same exterior surface area. The increase of the area ratio therefore leads to a higher steady-state temperature in the short stack.

The elevated temperatures increase the ionic conductivity of the Sustainion membrane and thereby decrease the ionic resistance in the individual cells. As the electrolyte temperature increase in the short stack is more pronounced with increasing current density, the voltages of the individual cells are lower at

https://doi.org/10.1021/acssuschemeng.4c00630
ACS Sustainable Chem. Eng. 2024, 12, 3876−3885

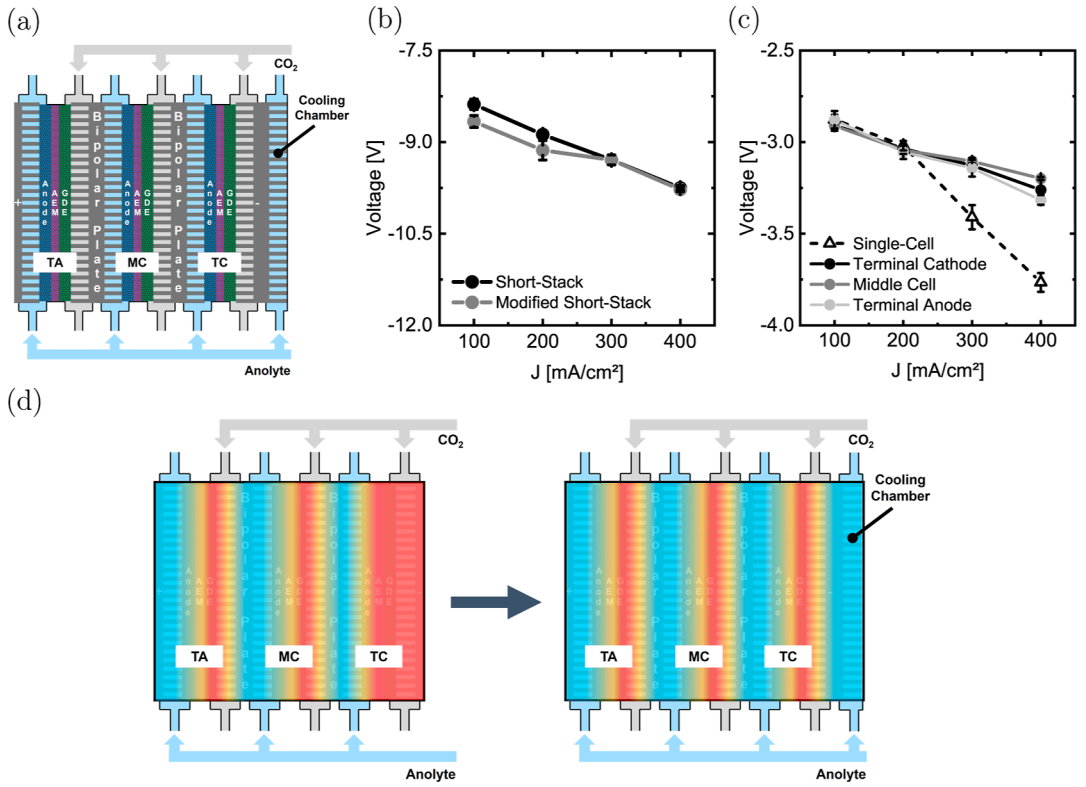

Figure 5. (a) Modified short stack with a half-plate of the bipolar plate on the adjacent side of the TC, (b) voltages obtained with a modified short stack and short stack, (c) cell voltages of individual cells in the modified short stack over different current densities, and (d) possible heat distribution in the short stack (left) and in the modified short stack (right) with neglected cooling by gas. Temperatures that are higher than the electrolyte temperature are colored in red, and the electrolyte temperature is colored in blue.

higher current densities compared to the voltage of the single cell.

To verify this hypothesis, an experiment at different current densities was performed with the single cell, where the electrolyte was heated to the electrolyte temperatures determined in experiments with the short stack at the specific current density. The electrolyte was heated to 30 °C at 100 mA/cm^2, to 33 °C at 200 mA/cm^2, to 38 °C at 300 mA/cm^2, and to 43 °C at 400 mA/cm^2. In Figure 4c, three times the cell voltage of the single cell obtained at ambient conditions and with the heated electrolyte as well as the short-stack voltage are presented over the different current densities.

Similar to the previous experiments at different current densities, the cell voltage increases with increasing current densities. The voltage increases from 2.85 V at 100 mA/cm^2 to 3.35 V at 400 mA/cm^2 (Figure 4c). While the voltages obtained in the experiments with the single cell are similar at 100 and at 200 mA/cm^2, lower voltages are observed at higher current densities for the single cell operated with the heated electrolyte. As illustrated in Figure 4c, the multiplied voltages of the single cell almost replicate the voltages obtained with the short stack. Thus, the single cell with the heated electrolyte operates at voltages similar to the average voltage of the individual cells in the short stack. For a more detailed description of the temperature effects on the cell, the Nyquist plots obtained for 33 and 38 °C at 300 mA/cm^2 with an excitation amplitude of 300 mA are presented in Figure 4d. In the Nyquist plots, a shift of the HFR from 0.86 Ω·cm^2 to 0.79 Ω·cm^2 can be observed. Since the HFR can be attributed to the membrane resistance,[44,45] a reduction of cell voltage with increasing temperature can be traced to membrane conductivity. A similar observation can be made for HFR values obtained in experiments at the other current densities (Table 1). In Figure 4d, a shift of the low-frequency resistance from 1.52 Ω·cm^2 to 1.48 Ω·cm^2 can be observed with increasing temperature, which is attributed to the charge-transfer reactions.[44,45] The Nyquist plots for the other current densities applied to the single cell as well as the Nyquist plots obtained for the short stack are presented in Figures S4 and S5 in the Supporting Information.

Overall, the results obtained with the heated electrolyte demonstrate that the reduced voltages in the short stack at higher current densities originate from higher temperatures in the short stack, influencing the membrane conductivity as well as the charge transfer.

Furthermore, these results allow the conclusion that the heat distribution in the short stack generates the reduction of cell voltage in the TC. The anticipated heat distribution of the short stack is the accumulation of heat in the middle of the short stack. Following this hypothesis, the highest temperatures and lowest cell voltages were to be determined for the MC and not, as observed in this work, for the TC. The cells making up the short stack are very asymmetrical, having a liquid and a gas side, when compared to, e.g., PEM-electrolysis cells where a liquid medium flows through both sides. If we ignore the minimal cooling effects by the gas, the cooling of the short stack only occurs via the electrolyte, and the highest temperatures in the cells of the short stack appear toward the cathode side of the MEA. While the TA and the MC are cooled by their anolytes and by the respective anolytes of their adjacent cells, the TC is cooled only by its anolyte and is, therefore, the only cell with liquid cooling from only one side.

https://doi.org/10.1021/acssuschemeng.4c00630
ACS Sustainable Chem. Eng. 2024, 12, 3876−3885

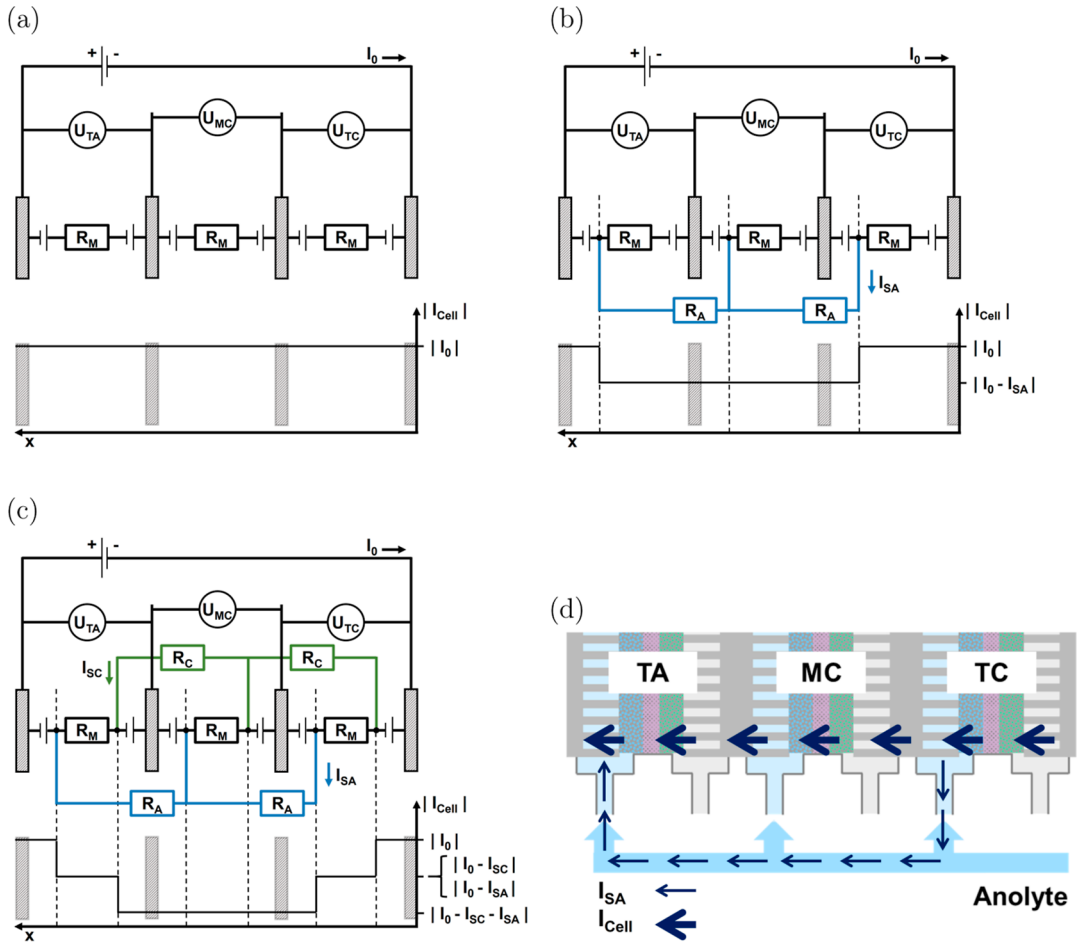

Figure 6. Circuit diagrams and graphs describing behavior of the current (I_{cell}) in the short stack for three-cell short stacks with (a) separate electrolyte circuits for each individual cell in the short stack to prevent shunt current formation, a (b) joint anolyte circuit for an entire short stack with an ionically conductive anolyte and no catholyte, and (c) two electrolyte circuits for the ionically conductive anolyte and catholyte. (d) Illustration of shunt current formation in the anolyte for the investigated short stack. (Membrane resistance: R_M; anolyte and catholyte resistance: R_A and R_C; voltages of individual cells: U_{TA}, U_{MC}, and U_{TC}; initial current: I_0; shunt currents in the anolyte and catholyte: I_{SA}, I_{SC}.)

Hence, higher temperatures can be expected to appear in the TC resulting in the observed lower cell voltages. The performance of the individual cells is therefore influenced by their location in the short stack.

To verify the hypothesis that the lower voltages determined for the TC arise from the asymmetrical heat distribution in the short stack, an experiment with a modified short stack is performed. The modularity of the bipolar plates enables the attachment of a half-bipolar plate on the TC (Figure 5a). This additional compartment is a media flow chamber for the electrolyte to cool the TC. An experiment is performed at the current densities of 100, 200, 300, and 400 mA/cm^2. Figure 5b depicts the voltages of the short stack and the modified short stack over the current densities. The voltages for the short stacks behave similarly with increasing current density; however, at lower current densities (100−200 mA/cm^2), higher voltages can be observed for the modified short stack. In Figure 5c, the obtained cell voltages of the individual cells in the short-stack and the single-cell voltage of the previous experiment are illustrated over the different current densities. As in previous experiments, the individual cell voltages are similar to the single-cell voltage at current densities of 100 and 200 mA/cm^2 (2.85 V at 100 mA/cm^2 and 3 V at 200 mA/cm^2). At higher current densities, lower cell voltages are determined for the individual cells compared to the single cell. The cell voltages of the individual cells are similar at 300 mA/cm^2 (3.15 V) but diverge at 400 mA/cm^2. While for the TA, a cell voltage of 3.31 V is determined at 400 mA/cm^2, for the TC and the MC, lower cell voltages with 3.25 and 3.2 V are observed.

Regarding the voltages of the short stacks, the additional cooling in the modified short stack can mitigate the temperature development in the short stack, which leads to the increase in voltage observed in Figure 5b. In terms of the individual cells, between 100 and 300 mA/cm^2, the voltage of the modified short stack is more evenly distributed on the individual cells compared to the short stack without additional cooling (Figure 3c). The additional chamber enables heat removal at the TC similar to the other individual cells and thereby generates a more symmetrical heat distribution in the short stack. In Figure 5d, the anticipated heat distributions in the short stack and the modified short stack are illustrated. Colored in red are temperatures higher than the electrolyte temperature, which is colored in blue. While the asymmetrical heat distribution in the short stack can reduce the cell voltage of the TC, thereby enhancing its performance, we emphasize that an asymmetrical heat distribution within the short stack can lead to different degradation processes in the individual

https://doi.org/10.1021/acssuschemeng.4c00630
ACS Sustainable Chem. Eng. 2024, 12, 3876−3885

cells. Considering this, the asymmetrical heat distribution is not beneficial, specifically in terms of possible long-term operation. However, this degradation behavior would be highly dependent on the specific materials used in the electrodes and membranes and thus is not explored in this study.

Due to symmetrical heat distribution, the individual cells operate at similar temperatures in the modified short stack; hence, similar cell voltages are obtained between 100 and 300 mA/cm^2. It is noteworthy that at 400 mA/cm^2, the individual cell voltages diverge within the standard deviations (±0.3 V). However, it is plausible that shunt currents form in the short stack, which can lead to an uneven voltage distribution within the short stack. As temperature effects in the modified short stack no longer dominate the voltage distribution in the short stack, the observation of shunt currents at higher current densities is possible and needs, therefore, to be investigated.

Shunt Current Effects. For a detailed description of shunt current effects in short stacks, circuit diagrams of three-cell short stacks are illustrated in Figure 6.

The depicted short stacks operate:

(a) with individual electrolyte circuits for each individual cell,

(b) with one joint anolyte circuit for all individual cells and no catholyte or with one joint anolyte circuit for all individual cells and individual catholyte circuits for all individual cells,

(c) with one joint anolyte circuit for all individual cells and one joint catholyte circuit for all individual cells.

The anolyte circuit is illustrated in blue, and the catholyte circuit is in green. The diagrams in Figure 6a–c depict the measuring locations for the TA, MC, and TC voltages (U_{TA}, U_{MC}, and U_{TC}) and provide the position of the membrane resistance (R_M) as well as the resistance of the anolyte and catholyte (R_C and R_A). The chemical reactions at the anode and cathode are illustrated as voltage sources. This representation was chosen instead of a (nonlinear) resistor to reflect the negligible change in electric potential observed in the experiment. Furthermore, for every circuit diagram, the absolute value of the current passing through the short stack (I_{cell}) is schematically illustrated over the length of the short stack.

In scenario (a), the initial current (I_0) enters the short stack at the cathode of the TC and flows through the short stack to exit the short stack at the anode of the TA. Hence, I_{cell} is similar to I_0 along the entire short-stack length, leading to a constant current density in the short stack. Therefore, in scenario (a), U_{TA}, U_{MC}, and U_{TC} are equal.

When operating with one anolyte circuit and an ionically conductive anolyte, I_{cell} is divided to a certain extent at the entrance and exit of the anolyte. The anolyte provides a bypass for the current, resulting in the formation of the parasitic shunt current I_{SA} at the anode of the TC. The shunt current follows the anolyte to re-enter the short stack at the anode of the TA. Corresponding to this scenario, I_{cell} is lower than I_0 between the anode of the TC and the anode of the TA, and the lowest load occurs in the middle of the short stack. Therefore, when shunt currents form in scenario (b), U_{TA} and U_{TC} possess a higher absolute value than U_{MC}.

In a short stack operating with one anolyte and one catholyte circuit, both containing ionically conductive media, the formation of shunt currents can have an even higher impact. As illustrated in the circuit diagram in Figure 6c, the catholyte provides an additional bypass to the one provided by the anolyte. At the entrance and exit of the catholyte, I_{SC} forms from I_{cell} and similar to scenario (b), I_{SA} forms in the anolyte. The impact on I_{cell} can therefore be even greater than that in scenario (b). Only at the anode of the TA and at the cathode of the TC is I_{cell} equal to I_0. The cell voltage behavior for scenarios (b) and (c) is the same with U_{MC} showing lower values than U_{TA} and U_{TC}.

Regarding the application these three scenarios are representing, scenario (a) is an operation mode that can prevent the formation of shunt currents but is associated with a significant increase of effort to set up the periphery and has therefore not been applied in this work. Nevertheless, the behavior of I_{cell} for scenario (a) represents the desired case for the presented three-cell short stack. Scenario (c) can describe the shunt current formation in chlor-alkali electrolyzer stacks or the shunt current formation in CO_2 electrolyzer stacks with cell architectures operating with a catholyte and an anolyte, similar to the one presented in our previous work.[33] In this work, the short stack does not operate with a catholyte, and the media flow channels connecting the cathodes in parallel are filled with a nonconductive medium (CO_2 gas). Hence, scenario (b) is the most likely to appear in the presented system and is, therefore, additionally illustrated in Figure 6d. The illustration depicts I_{cell} and I_{SA} flowing through the short stack and the anolyte. Displayed is only the bottom half of the short stack, as the bubble formation (O_2/CO_2) appearing at the anode prevents the formation of shunt currents toward the exit of the anolyte.

The individual cell voltages observed in the experiments with the modified short stack at 400 mA/cm^2 (Figure 5b) display a possible voltage distribution expected for scenario (b) (Figure 6b). Here, at 400 mA/cm^2, a lower cell voltage is observed for the MC compared to the TA and TC. To quantify possible shunt currents in the short stack, an experiment is performed with a short stack in which the MEAs are replaced by PTFE sheets. Hence, the bipolar plates and end plates were only connected via the ionically conductive anolyte. Cyclic voltammetry between 0 and 10 V was performed. The potential was applied between the anode plate of the TC and the anode plate of the TA. A detailed description and a plot with the results of the cyclic voltammetry experiments are presented in Figure S6 in the Supporting Information. At a voltage of 6.6 V, which has been the highest determined voltage between the two anode plates in experiments with the MEAs (Figure 3c), a current of 0.4 mA (at 45 °C) was observed. Hence, it is likely that shunt currents appear within the short stack, which contributes to the voltage distribution in the modified short stack at 400 mA/cm^2. However, considering the ratio of the determined shunt current to the applied current densities in experiments with the short stack, the shunt current formation is negligible.

CONCLUSIONS

In this work, the design of a three-cell short stack for the CO_2-to-CO electrolysis operating with MEA cells is reported, and its performance is compared to that of its equivalent single cell.

The short stack was assembled with modular bipolar plates, allowing the measurement of the individual cell voltages within the short stack, thereby enabling the comparison of the individual cell performances to the single-cell performance.

A difference between the performance of the individual cells and that of the single cell was observed. While the FE(CO)

https://doi.org/10.1021/acssuschemeng.4c00630
ACS Sustainable Chem. Eng. 2024, 12, 3876−3885

values of the short stack and the single cell were similar, the cell voltages for the individual cells were lower than for the single cells. It was demonstrated that elevated temperatures occurring in the short stack enhanced the ionic conductivity of the membrane and the charge transfer, leading to decreasing individual cell voltages compared to the single cell. This effect became more pronounced with increasing current densities.

It is noteworthy that the measurement of the individual cell voltages revealed the correlation between each cell's performance and its position in the short stack. By exploiting the flexibility of our short-stack design, we were able to trace the cell voltage reduction of the TC to temperature gradients within the short stack.

With the reported results, the adaptable short-stack design moves the CO_2-to-CO electrolysis closer to a scale-up and allows an initial estimation of the cells' behavior in a scaled process.

■ ASSOCIATED CONTENT

Supporting Information

The Supporting Information is available free of charge at https://pubs.acs.org/doi/10.1021/acssuschemeng.4c00630.

> Description of the experimental process design for the short stack and single cell, list of materials, and description of gas analytics, total Faraday efficiency over current density for the short stack and single cell, results of EIS measurements, results of shunt current quantification, and results of ^{1}H NMR analysis measurement of the anolyte (PDF)

■ AUTHOR INFORMATION

Corresponding Authors

Maximilian Quentmeier − *Institute of Physical Chemistry, RWTH Aachen University, 52074 Aachen, Germany; Institute of Energy and Climate Research, Forschungszentrum Jülich GmbH, 52425 Jülich, Germany;* orcid.org/0000-0003-0495-9414; Email: m.quentmeier@fz-juelich.de

Bernhard Schmid − *Institute of Energy and Climate Research, Forschungszentrum Jülich GmbH, 52425 Jülich, Germany*; Email: b.schmid@fz-juelich.de

Authors

Hermann Tempel − *Institute of Energy and Climate Research, Forschungszentrum Jülich GmbH, 52425 Jülich, Germany;* orcid.org/0000-0002-9794-6403

Rüdiger-A. Eichel − *Institute of Physical Chemistry, RWTH Aachen University, 52074 Aachen, Germany; Institute of Energy and Climate Research, Forschungszentrum Jülich GmbH, 52425 Jülich, Germany;* orcid.org/0000-0002-0013-6325

Complete contact information is available at: https://pubs.acs.org/10.1021/acssuschemeng.4c00630

Notes

The authors declare no competing financial interest.

■ ACKNOWLEDGMENTS

The authors kindly acknowledge funding by the Federal Ministry of Education and Research (BMBF), Project: iNEW2.0 'Inkubator Nachhaltige Elektrochemie' Funding code: 03SF0627A. The support of Marcel Turiaux in the development of the cell design and the support of Michael Schatz in NMR measurements are gratefully acknowledged.

■ REFERENCES

(1) Dinh, C.-T.; García de Arquer, F. P.; Sinton, D.; Sargent, E. H. High Rate, Selective, and Stable Electroreduction of CO_2 to CO in Basic and Neutral Media. *ACS Energy Lett.* **2018**, *3*, 2835−2840.

(2) Baessler, J.; Oliveira, T.; Keller, R.; Wessling, M. Paired Electrosynthesis of Formic Acid from CO_2 and Formaldehyde from Methanol. *ACS Sustainable Chem. Eng.* **2023**, *11*, 6822−6828.

(3) Endrődi, B.; Bencsik, G.; Darvas, F.; Jones, R.; Rajeshwar, K.; Janáky, C. Continuous-flow electroreduction of carbon dioxide. *Prog. Energy Combust. Sci.* **2017**, *62*, 133−154.

(4) Bell, D.; Rall, D.; Großeheide, M.; Marx, L.; Hülsdünker, L.; Wessling, M. Tubular hollow fibre electrodes for CO_2 reduction made from copper aluminum alloy with drastically increased intrinsic porosity. *Electrochem. Commun.* **2020**, *111*, 106645.

(5) Higgins, D.; Hahn, C.; Xiang, C.; Jaramillo, T. F.; Weber, A. Z. Gas-Diffusion Electrodes for Carbon Dioxide Reduction: A New Paradigm. *ACS Energy Lett.* **2019**, *4*, 317−324.

(6) Kaczur, J. J.; Yang, H.; Liu, Z.; Sajjad, S. D.; Masel, R. I. Carbon Dioxide and Water Electrolysis Using New Alkaline Stable Anion Membranes. *Front. Chem.* **2018**, *6*, 263.

(7) Küngas, R. Review—Electrochemical CO_2 Reduction for CO Production: Comparison of Low- and High-Temperature Electrolysis Technologies. *J. Electrochem. Soc.* **2020**, *167*, 044508.

(8) Brée, L. C.; Wessling, M.; Mitsos, A. Modular modeling of electrochemical reactors: Comparison of CO_2-electolyzers. *Comput. Chem. Eng.* **2020**, *139*, 106890.

(9) Heßelmann, M.; Bräsel, B. C.; Keller, R. G.; Wessling, M. Simulation-based guidance for improving CO_2 reduction on silver gas diffusion electrodes. *Electrochem. Sci. Adv.* **2023**, *3*, 2100160.

(10) Corson, E. R.; Subramani, A.; Cooper, J. K.; Kostecki, R.; Urban, J. J.; McCloskey, B. D. Reduction of carbon dioxide at a plasmonically active copper−silver cathode. *Chem. Commun.* **2020**, *56*, 9970−9973.

(11) Masel, R. I.; Liu, Z.; Yang, H.; Kaczur, J. J.; Carrillo, D.; Ren, S.; Salvatore, D.; Berlinguette, C. P. An industrial perspective on catalysts for low-temperature CO_2 electrolysis. *Nat. Nanotechnol.* **2021**, *16*, 118−128.

(12) Reichbauer, T.; Schmid, B.; Vetter, K.-M.; Reinisch, D.; Martić, N.; Reller, C.; Grasruck, A.; Dorta, R.; Schmid, G. Electrical energy input efficiency limitations in CO_2-to-CO electrolysis and attempts for improvement. *Electrochem. Sci. Adv.* **2023**, No. e2300024.

(13) Kutz, R. B.; Chen, Q.; Yang, H.; Sajjad, S. D.; Liu, Z.; Masel, I. R. Sustainion Imidazolium-Functionalized Polymers for Carbon Dioxide Electrolysis. *Energy Technol.* **2017**, *5*, 929−936.

(14) Endrődi, B.; Kecsenovity, E.; Samu, A.; Darvas, F.; Jones, R. V.; Török, V.; Danyi, A.; Janáky, C. Multilayer Electrolyzer Stack Converts Carbon Dioxide to Gas Products at High Pressure with High Efficiency. *ACS Energy Lett.* **2019**, *4*, 1770−1777.

(15) Endrődi, B.; Kecsenovity, E.; Samu, A.; Halmágyi, T.; Rojas-Carbonell, S.; Wang, L.; Yan, Y.; Janáky, C. High carbonate ion conductance of a robust PiperION membrane allows industrial current density and conversion in a zero-gap carbon dioxide electrolyzer cell. *Energy Environ. Sci.* **2020**, *13*, 4098−4105.

(16) Kutlusoy, T.; Divanis, S.; Pittkowski, R.; Marina, R.; Frandsen, A.; Minhova-Macounova, K.; Nebel, R.; Zhao, D.; Mertens, S. F. L.; Hoster, H.; Krtil, P.; Rossmeisl, J. Synergistic effect of p-type and n-type dopants in semiconductors for efficient electrocatalytic water splitting. *Chem. Sci.* **2022**, *13*, 13879−13892.

(17) Kostecki, R.; Augustynski, J. Electrochemical reduction of CO_2 at an activated silver electrode. *Ber. Bunsenges. Phys. Chem.* **1994**, *98*, 1510−1515.

(18) Vennekötter, J.-B.; Scheuermann, T.; Sengpiel, R.; Wessling, M. The electrolyte matters: Stable systems for high rate electrochemical CO_2 reduction. *J. CO_2 Util.* **2019**, *32*, 202−213.

(19) Vennekoetter, J.-B.; Sengpiel, R.; Wessling, M. Beyond the catalyst: How electrode and reactor design determine the product

spectrum during electrochemical CO_2 reduction. *Chem. Eng. J.* **2019**, *364*, 89−101.
(20) Delacourt, C.; Ridgway, P.; Kerr, J.; Newman, J. Design of an Electrochemical Cell Making Syngas (CO + H_2) from CO_2 and H_2O Reduction at Room Temperature. *J. Electrochem. Soc.* **2008**, *155*, B42.
(21) Larrazábal, G. O.; Strøm-Hansen, P.; Heli, J. P.; Zeiter, K.; Therkildsen, K. T.; Chorkendorff, I.; Seger, B. Analysis of Mass Flows and Membrane Cross-over in CO_2 Reduction at High Current Densities in an MEA-Type Electrolyzer. *ACS Appl. Mater. Interfaces* **2019**, *11*, 41281−41288.
(22) Reinisch, D.; Schmid, B.; Martić, N.; Krause, R.; Landes, H.; Hanebuth, M.; Mayrhofer, K. J. J.; Schmid, G. Various CO_2-to-CO Electrolyzer Cell and Operation Mode Designs to avoid CO_2-Crossover from Cathode to Anode. *Z. Phys. Chem.* **2020**, *234*, 1115−1131.
(23) Li, T.; Lees, E. W.; Goldman, M.; Salvatore, D. A.; Weekes, D. M.; Berlinguette, C. P. Electrolytic Conversion of Bicarbonate into CO in a Flow Cell. *Joule* **2019**, *3*, 1487−1497.
(24) Li, Y. C.; Zhou, D.; Yan, Z.; Gonçalves, R. H.; Salvatore, D. A.; Berlinguette, C. P.; Mallouk, T. E. Electrolysis of CO_2 to Syngas in Bipolar Membrane-Based Electrochemical Cells. *ACS Energy Lett.* **2016**, *1*, 1149−1153.
(25) Salvatore, D. A.; Weekes, D. M.; He, J.; Dettelbach, K. E.; Li, Y. C.; Mallouk, T. E.; Berlinguette, C. P. Electrolysis of Gaseous CO_2 to CO in a Flow Cell with a Bipolar Membrane. *ACS Energy Lett.* **2018**, *3*, 149−154.
(26) Weekes, D. M.; Salvatore, D. A.; Reyes, A.; Huang, A.; Berlinguette, C. P. Electrolytic CO_2 Reduction in a Flow Cell. *Acc. Chem. Res.* **2018**, *51*, 910−918.
(27) Martens, C.; Schmid, B.; Tempel, H.; Eichel, R.-A. CO_2 flow electrolysis − limiting impact of heat and gas evolution in the electrolyte gap on current density. *Green Chem.* **2023**, *25*, 7794−7806.
(28) Liang, S.; Altaf, N.; Huang, L.; Gao, Y.; Wang, Q. Electrolytic cell design for electrochemical CO_2 reduction. *J. CO_2 Util.* **2020**, *35*, 90−105.
(29) Rabinowitz, J. A.; Kanan, M. W. The future of low-temperature carbon dioxide electrolysis depends on solving one basic problem. *Nat. Commun.* **2020**, *11*, 5231.
(30) Mardle, P.; Cassegrain, S.; Habibzadeh, F.; Shi, Z.; Holdcroft, S. Carbonate Ion Crossover in Zero-Gap, KOH Anolyte CO_2 Electrolysis. *J. Phys. Chem. C* **2021**, *125*, 25446−25454.
(31) Jouny, M.; Luc, W.; Jiao, F. General Techno-Economic Analysis of CO_2 Electrolysis Systems. *Ind. Eng. Chem. Res.* **2018**, *57*, 2165−2177.
(32) Krause, R.; Reinisch, D.; Reller, C.; Eckert, H.; Hartmann, D.; Taroata, D.; Wiesner-Fleischer, K.; Bulan, A.; Lueken, A.; Schmid, G. Industrial Application Aspects of the Electrochemical Reduction of CO_2 to CO in Aqueous Electrolyte. *Chem. Ing. Tech.* **2020**, *92*, 53−61.
(33) Quentmeier, M.; Schmid, B.; Tempel, H.; Kungl, H.; Eichel, R.-A. Toward a Stackable CO_2-to-CO Electrolyzer Cell Design - Impact of Media Flow Optimization. *ACS Sustainable Chem. Eng.* **2023**, *11*, 679−688.
(34) Teuku, H.; Alshami, I.; Goh, J.; Masdar, M. S.; Loh, K. S. Review on bipolar plates for low−temperature polymer electrolyte membrane water electrolyzer. *Int. J. Energy Res.* **2021**, *45*, 20583−20600.
(35) Rizwan, M.; Alstad, V.; Jäschke, J. Design considerations for industrial water electrolyzer plants. *Int. J. Hydrogen Energy* **2021**, *46*, 37120−37136.
(36) Burney, H. S.; White, R. E. Predicting Shunt Currents in Stacks of Bipolar Plate Cells with Conducting Manifolds. *J. Electrochem. Soc.* **1988**, *135*, 1609−1612.
(37) O'Brien, T. F.; Bommaraju, T. V.; Hine, F. *Handbook of Chlor-Alkali Technology*; Springer: New York, 2005.
(38) Haas, T.; Krause, R.; Weber, R.; Demler, M.; Schmid, G. Technical photosynthesis involving CO_2 electrolysis and fermentation. *Nat. Catal.* **2018**, *1*, 32−39.
(39) Liu, Z.; Yang, H.; Kutz, R.; Masel, R. I. CO_2 Electrolysis to CO and O_2 at High Selectivity, Stability and Efficiency Using Sustainion Membranes. *J. Electrochem. Soc.* **2018**, *165*, J3371−J3377.
(40) Fortin, P.; Khoza, T.; Cao, X.; Martinsen, S. Y.; Oyarce Barnett, A.; Holdcroft, S. High-performance alkaline water electrolysis using Aemion anion exchange membranes. *J. Power Sources* **2020**, *451*, 227814.
(41) Ziv, N.; Dekel, D. R. A practical method for measuring the true hydroxide conductivity of anion exchange membranes. *Electrochem. Commun.* **2018**, *88*, 109−113.
(42) Garg, S.; Giron Rodriguez, C. A.; Rufford, T. E.; Varcoe, J. R.; Seger, B. How membrane characteristics influence the performance of CO_2 and CO electrolysis. *Energy Environ. Sci.* **2022**, *15*, 4440−4469.
(43) Długołęcki, P.; Ogonowski, P.; Metz, S. J.; Saakes, M.; Nijmeijer, K.; Wessling, M. On the resistances of membrane, diffusion boundary layer and double layer in ion exchange membrane transport. *J. Membr. Sci.* **2010**, *349*, 369−379.
(44) Mardle, P.; Gangrade, A.; Saatkamp, T.; Jiang, Z.; Cassegrain, S.; Zhao, N.; Shi, Z.; Holdcroft, S. Performance and Stability of Aemion and Aemion+ Membranes in Zero-Gap CO_2 Electrolyzers with Mild Anolyte Solutions. *ChemSusChem* **2023**, *16*, No. e202202376.
(45) Lazanas, A. C.; Prodromidis, M. I. Electrochemical Impedance Spectroscopy-A Tutorial. *ACS Meas. Sci. Au* **2023**, *3*, 162−193.

https://doi.org/10.1021/acssuschemeng.4c00630
ACS Sustainable Chem. Eng. 2024, 12, 3876−3885